Isolation and *In silico* prediction of potential drug-like compounds with a new dimeric prenylated quinolone alkaloid from *Zanthoxylum rhetsa* (Roxb.) root extracts targeted against SARS-CoV-2 (Mpro)

Fatema -Tuz- Zohora (fatema.zohora41@gmail.com)
PAU: Primeasia University https://orcid.org/0000-0002-6087-0425
Sinthyia Ahmed
Red and Green Practice
Khondaker Miraz Rahman
King's College
Mohammad A. Halim
Kennesaw State University
Md. Rafi Anwar
ULM: The University of Louisiana Monroe
Md. Hossain Sohrab
BCSIR: Bangladesh Council of Scientific and Industrial Research
Fatema Tabassum
Northern University Bangladesh
Choudhury Mahmood Hasan
University of Dhaka: Dhaka University
Monira Ahsan
University of Dhaka: Dhaka University

Research Article

Keywords: Zanthoxylum rhetsa, 2,11-didemethoxy-vepridimerine A, SARS-CoV-2 (Mpro), 2-quinolone, benzophenanthridine alkaloids

Posted Date: May 25th, 2022

DOI: https://doi.org/10.21203/rs.3.rs-1678790/v1

Abstract

A new dimeric prenylated quinolone alkaloid, named 2,11-didemethoxy-vepridimerine A, was isolated from the root bark of *Zanthoxylum rhetsa*, together with thirteen known compounds. The structure of the new compound was elucidated on the basis of spectroscopic investigations (NMR and Mass). The interaction of the isolated compounds with the main protease of SARS-CoV-2 (Mpro) was evaluated using molecular docking followed by MD simulations. The result suggests that 2, 11-didemethoxy-vepridimerine A, the new compound has the highest negative binding affinity against the Mpro with free energy of binding of-8.5 Kcal/mol indicating interaction with the Mpro. This interaction was further validated with the help of MD simulation using remdesivir, one of the currently approved drugs against SARS-CoV-2, as a control.

Introduction

COVID-19 is caused by SARS-CoV-2 which is a highly contagious novel coronavirus. There is an urgent clinical need to find new antiviral agents against SARS-CoV-2 as, except the recently approved paxlovid from Pfizer and some repurposed drugs like remdesivir and favirapiravir, there is no approved directly acting antiviral drug that works against SARS-CoV-2 targets. Viral diseases initiated by Coronavirus (CoV) have become the major public health problems worldwide in the last two decades. The recent emergence of the deadly COVID-19 due to SARS-CoV-2 has created unprecedented pandemic situations around the globe making the need for antiviral molecules to treat it (Jafrin Jobayer et al. 2021), (Sharma et al. 2020). Natural products and herbal medicines provide a unique dimension in the drug development methods for antiviral medication (REF). From a drug discovery point of view, active ingredients extracted from natural products usually possess exceptional novelty in structures with intrinsic pharmacological activities. Many studies on natural products with the antiviral effect shed light on some bioactive ingredients' potential against various viral diseases. (Jafrin Jobayer *et al.* 2021), (Thomford et al. 2018), (Osakwe et al. 2016). The effectiveness of computational aided drug design as one of the versatile tools for facilitating drug discovery and development has been recognized for last decades, especially, in the case of natural products (Osakwe et al. 2016), (Thomford et al. 2018), (Atanasov et al. 2015). A number of of plant secondary metabolites such as glycyrrhizin, baicalin and quercetin that have been studied *in silico* and found to have antiviral and anti-SARS-Cov activity (Yonesi & Rezazadeh 2020). Furthermore, the family *Rutaceae* is known for generating a large variety of secondary metabolites, like phenanthridine, acridone and furo- and pyranoquinoline alkaloids, complicated furo- and pyranocoumarins, flavonoids and numerous sorts of terpinoids, together with the limonoids (Haque et al. 2013) that have shown a range of pharmacological activities. The main objective of the present work was the isolation and structural determination of new secondary metabolites present in the root bark of *Zanthoxylum rhetsa* (Roxb.) DC and evaluate their ability to inhibit the SARS-CoV-2 Mpro using *in silico* techniques.

Simulations were performed using the YASARA software package for new compound **1** along with the apo form and a standard drug, Remdesivir (Krieger et al. 2004).

Materials And Methods

General Experimental Procedures

In the present work, NMR spectra were measured at 400 MHz for ^{1}H NMR spectra and 100 MHz for ^{13}C on a Bruker 400™ ASCEND spectrometers. The sample was dissolved in $CDCl_3$ and TMS was used as internal standard ($\delta_C = 0$). Chemical shifts are expressed in a δ (ppm) scale with tetramethylsilane and/or residual solvents as internal reference and coupling constants (*J*) are in hertz. High resolution electrospray ionization mass spectrometry (HRESIMS) was used for obtaining the mass spectrum. Column chromatography (CC) was carried out using powdered silica gel 60 H (Kieselgel 60, mesh 70–230). The glass column having a length of 92 cm and diameter 4.5 cm was packed with silica gel. Thin layer chromatography (TLC) was obtained using pre-coated silica gel plates (silica gel 60 F254, aluminium sheets, E-Merck, Germany) and the established chromatogram was detected under UV light (366 nm and 254 nm) and glowing and quenched spots were marked and then the recognition was visualized by spraying with Vanillin-H_2SO_4 and modified Dragendorff's reagent.

Plant Material

The root bark of *Zanthoxylum rhetsa* was collected from Dhaka, Narsingdi district of Bangladesh in August 2013. The plants were identified by an expert at the Bangladesh National Herbarium and where a voucher specimen was deposited (DACB accession number is 42528). The plant parts were cleaned properly. The parts were cut into small pieces and subjected to shade drying for a week. The dried plant part was then crushed into coarse powder by a high capacity grinding machine with proper care.

Extraction and Isolation

The powdered root bark of *Zanthoxylum rhetsa* (3.5 kg) was soaked in MeOH (5 L) at room temperature for two weeks. The MeOH extracts were combined and evaporated in vacuum to yield a dark brown residue (40 gm, semi-dry). The crude extract was then fractionated sequentially with petroleum ether (9 g, PE), ethyl acetate (5 g, EtOAc) and chloroform (12 g, $CHCl_3$) by continuous stirring. The $CHCl_3$ soluble fraction (12 g) was subjected to column chromatography (CC) over silica gel [PE- CH_2Cl_2 gradient (100:0–0:100, v/v) to CH_2Cl_2-EtOAc (99:1–0:100, v/v) to EtOAc-MeOH (99:1–0:100, v/v)] to afford 700 fractions each with 20 ml solution. Based on TLC screening, fractions 34 to 40 (EtOAc-CH_2Cl_2, 32:68, v/v), 41 to 45 (EtOAc-CH_2Cl_2, 34:66, v/v), 46 to 56 (EtOAc-CH_2Cl_2, 34:66 – 36:64, v/v), 60 to 62 (EtOAc-CH_2Cl_2, 36:64, v/v), 89 to 90 (EtOAc-CH_2Cl_2, 44:56, v/v) and 175 to 176 (MeOH-EtOAc, 15:85 – 18:82, v/v) were combined, giving six subfractions (Fr.1-Fr.6). All the subfractions were further fractionated by gel permeation chromatography with sephadex LH-20 using petroleum ether/chloroform (20:80, v: v) to afford 1 to 20 subfractions, containing 1.5 ml each. After TLC analysis subfractions Fr.3.7-Fr.3.10 are mixed together followed by TLC eluting with toluene/ EtOAc (90:10) to come up compound 1 (9 mg, R_f = 0.40), the sample containing TLC plate was run four times in the solvent system. Concentrated subfractions Fr.5.4–5.5 gave crystals and after recrystallization afforded found compound 7 (5 mg, R_f =

0.37). Subjected to TLC of subfraction Fr.6.3-Fr.6.6 eluting with toluene/ EtOAc (85:15, v/v) to afford mixture of compound 5 (4.5 mg, R_f = 0.49) and compound 6 (9 mg, R_f = 0.49).

The entire pet ether soluble fraction (9 g) was exposed to column chromatography (CC) by means of silica gel by gradient elution with pet ether/dichloromethane/ethyl acetate/methanol [PE- CH_2Cl_2 gradient (100:0–0:100, v/v) to CH_2Cl_2-EtOAc (99:1–0:100, v/v) to EtOAc-MeOH (99:1–0:100, v/v)] to afford 551 fractions each with 20 ml. The fractions 1 to 19 (Pet ether,100:0, v/v), the fractions 60 to 99 (CH_2Cl_2 in pet ether, 5:95 – 15:85,v/v),140 to 175 (CH_2Cl_2 in pet ether, 50:50–100:0), 219 to 279 (EtOAc in CH_2Cl_2, 15:85 – 25:75,v/v), 340 to 360 (EtOAc in CH_2Cl_2, 30:70–75:25,v/v), 370–410 (EtOAc in CH_2Cl_2, 80:70–100:0,v/v) and 480 to 551 (EtOAc in MeOH, 44:56,v/v) are mix together affording seven fractions (Fr.1-Fr.7) based on TLC analysis respectively. Fr.5 and Fr.7 were resubmitted to Sephadex LH-20 eluted with petroleum ether/chloroform (20:80, v: v) afforded another twenty sub fractions of each fraction. Fr.5.7-Fr.5.14 mixed together subjected to TLC run with toluene/ EtOAc (97:3, v/v) for three times to yield compound 2 (8.7 mg, R_f = 0.80) and compound 3 (8.7 mg, R_f = 0.80). Subfractions Fr.4.7-Fr.4.15 added together followed by subjected to TLC eluted with toluene/ EtOAc (97:3) to yield compound 8 (4.5 mg, R_f = 0.49). From Fr. 2 and Fr. 3 get compound 9 (20 mg, R_f = 0.55) and compound 10 (20 mg, R_f = 0.55). Fr.1 afforded compound 11 (8 mg, R_f = 0.46), compound 12 (8 mg, R_f = 0.47) and compound 13 (8 mg, R_f = 0.46) by TLC eluting with toluene/ EtOAc (95.5:0.5, v: v).

Methodologies of Molecular Docking on SARS-CoV-2 main proteases

Molecular docking

Optimization at semi-empirical PM6 method (gaseous phase) of the structure of the selected compounds was employed (Stewart, 2007). Later the vibrational frequencies were computed and the absence of imaginary frequencies confirmed the stationary points correspond to minima on the Potential Energy Surface. From the RCSB Protein Data Bank (PDB ID: 6LU7) the crystal structure of the Mpro was taken. After that it was energy minimized through Swiss PDB Viewer (Guex & Peitsch, 1997). PyMol (version 2.3.2) software package was used to eliminate all the hetero atoms, and water molecules present in the crystal structure (DeLano, 2002). Molecular docking between Mpro with thirteen compounds was performed by AutoDock Vina protocol for the potential interactions and activity predictions (Trott & Olson, 2010). The Mpro active site was set around in the docking grid box, where the center was around X = -9.83, Y = 14.38, Z = 68.48 and the dimensions were X: 24.69, Y: 31.64, and Z: 29.97. Finally, the non-covalent interaction in the docked drug-protein complex, PyMol and BIOVIA discovery studio (version 4.5) were visualized and detected.

Molecular dynamics

Along with the apo form and a standard drug, remdesivir, MD simulations of new compound 1 was performed using the YASARA software package (Krieger et al., 2004). These simulations were executed to study the virtual stability of the ligand locate in the binding pocket. A dynamics system consisted of one copy of Mpro, one copy of docked compound, water molecules, and 0.9% NaCl at 298K temperature. The entire system was neutralized. The MD system was first relaxed for a protein-ligand complex via a series of procedures such as the steepest descent minimization, simulated annealing minimization of the solvent. For describing the macromolecular system, the AMBER14 force field was utilized. Three-dimensional periodic boundary conditions (PBC) were applied wherever the cell size was 20 Å larger than the Mpro size in all cases. Throughout all simulations, the Particle-Mesh-Ewald (PME) method was employed for long-range electrostatic interactions (with a cut-off of 8 Å). The simulation temperature was controlled by Berendsen thermostat process. For performing 100 ns MD simulation a time step of 1.25 fs was maintained. The snapshots were taken at every 100 ps. Depending on previous MD data analysis process root-mean-square deviation (RMSD), root-mean-square fluctuation (RMSF), radius of gyration (Rg), and solvent accessible surface area (SASA), molecular surface area (MolSA), dihedral angle, and total number of hydrogen bonds data were retrieved from the MD simulations (Ahmed et al., 2020; Junaid et al., 2017; Shahinozzaman et al., 2019). At that point, 100 snapshot conformers were generated and saved in PDB format at every 1 ns of 100 ns MD simulation.

Binding energy calculation MM-PBSA

By using software YASARA gibbs free energy was calculated for analysing binding affinity of ligands. Interaction energy for Mpro with compound 1 and remdesivir were calculated. MM-PBSA methods were implemented for 51 to 100 ns.

Results

A methanol extract of the root bark of *Zanthoxylum rhetsa* afforded thirteen chemical compounds. Among them 2,11-didemethoxy-vepridimerine A (**1**) is a new dimeric prenylated quinolone alkaloid, N-methylatanine (**2**) and 3-dimethylallyl-4,8-dimethoxy-1-methyl-2-quinolone (**3**) 2-quinolone alkaloids isolated for the first time from the genus *Zanthoxylum*. 8-O-demethylchelerythrine (**4**), chelerythrine (**5**) earlier isolated from *Z. rhetsa* and 7-methoxynitidine (**6**) also appeared as a new natural compound, however it was synthesized previously, canthin-6-one (**7**), (+)-piperitol-γ-γ-dimethylallylether (**8**). stigmasterol (**9**), β-sitosterol (**10**), methyl oleate (**11**), methyl stearate (**12**) & stearic acid (**13**) a very common structures (Fig. 1), was also isolated and identified by comparison of their spectroscopic data with those reported in the literature.

Compound **1**, isolated as a yellowish mass, showed a blue fluorescent and quenching spot when examined under 366 nm and 254 nm UV light on a TLC plate and produced very light yellow color when sprayed with vanillin in sulphuric acid reagent followed by heating for 5 minutes. It gave orange red color after spraying with Dragendorff's reagent. The HRESIMS showed a peak at *m/z* 543.2480 (MH^+) measured in the positive ion mode and solved for the molecular formula $C_{32}H_{34}N_2O_6$. The ^1H NMR

spectrum (400 MHz, $CDCl_3$; Table 1) revealed two pairs of three adjacent aromatic protons at δ 7.05 dd (*J* = 8.0, 1.3 Hz), 7.17 dd (*J* = 7.9, 8.0 Hz), 7.63 dd (*J* = 7.9, 1.3 Hz) and δ 7.04 dd (*J* = 8.0, 1.3 Hz), 7.14 dd (*J* = 7.9, 8.0 Hz), 7.73 dd (*J* = 7.9, 1.3 Hz), two methoxy groups at δ 3.89 and 3.88 and two N-methyls at δ 3.93 and 3.88. In addition, the spectrum displayed three tertiary methyls at δ 1.55, 1.87 and 1.55 and seven aliphatic protons at δ 1.57 to 3.20 (Table 1). The ^{13}C NMR spectrum (Table 1) showed altogether thirty two carbons including two carbonyl carbons at δ 163.9 and 163.0. The spectrum, jointly with the HSQC spectrum, revealed carbons assigned to six aromatic methines, three aliphatic methines, two methylenes, two methoxyls, two N-methyls, three tertiary methyls, four saturated quaternary carbons (two being oxygenated) and eight aromatic/olefinic quaternary carbons. All these data were similar to those of vepridimerine A (Ngadjui et al. 1982) and (Ngadjui et al. 1992), except the absence of two methoxyl groups at C-2 and C-11. That is, compound **1** consists of two 8-methoxy-N-methyl quinolone units joined by a C_{10} moiety. The small coupling constant of 6.3 Hz between H_d and H_e suggested a *cis* relationship as in vepridimerine A (Table 1 and Table 2). The COSY, HSQC and HMBC spectra allowed assignment of all the carbons and protons in the molecule. The relative stereochemistry was confirmed by a NOESY experiment which showed crosspeaks between H_d & H_e, and also between H_b & H_c, H_b & H_g (Fig. 2**)**. On the basis of above data compound **1** was characterized as 2,11-didemethoxy-vepridimerine A. This is the first report of isolation of this alkaloid from a natural source.

Table 1
NMR spectral data (400 MHz, $CDCl_3$) for compound **1**.

Position	δ_H[a]	δ_C[b]	HSQC	HMBC
1	—	148.5		
2	7.05 dd (*J* = 8.0, 1.3 Hz)	114.1	114.1	130.6 (C-18a), 116.0 (C-4)
3	7.17 dd (*J* = 8.0, 7.9 Hz)	122.0	122.0	148.5 (C-1), 118.3 (C-4a)
4	7.63 dd (*J* = 7.9, 1.3 Hz)	116.0	116.0	c
4a	—	118.3		
4b	—	158.1		
6	—	80.0		
6a	2.23 d (*J* = 6.3 Hz)	43.5	43.5	c
7	3.70 br s	27.8	27.8	c
7a	—	108.3		
8	—	163.0		
9a	—	130.4		
10	—	148.3		
11	7.04 dd (*J* = 8.0, 1.3 Hz)	113.7	113.7	116.2 (C-13)
12	7.14 dd (*J* = 8.0, 7.9 Hz)	122.3	122.3	148.3 (C-10), 118.8 (C-13a)
13	7.73 dd (*J* = 7.9, 1.3 Hz)	116.2	116.2	
13a	—	118.8		
13b	—	154.9		
15	—	77.1		
16	1.57 t (*J* = 14.2 Hz) 3.20 ddd (*J* = 14.2, 5.5, 2.4 Hz)	39.5	39.5	

Table 1 **(Cont.)**. NMR spectral data (400 MHz, $CDCl_3$) for compound **1**.

Position	δ_H[a]	δ_C[b]	HSQC	HMBC
16a	3.05 ddd (*J* = 12.5, 6.0,5.7 Hz)	26.5	26.5	c
16b	—	109.7		

[a] = measured in 400 MHz, [b]= measured in 100 MHz, c = not observed

Position	δ_H[a]	δ_C[b]	HSQC	HMBC
17	—	163.9		
18a	—	130.6		
19	1.74 dt (*J* = 13.8, 2.5 Hz) 2.19 dd (*J* = 13.8, 2.8 Hz)	32.2	32.2	c
Me-6	1.55, 3H s	24.9	24.9	43.5 (C-6a), 29.2 (Me-6)
Me-6	1.87, 3H s	29.2	29.2	80.0(C-6), 43.5(C-6a), 24.9 (Me-6)
Me-15	1.55, 3H s	28.7	28.7	77.1(C-16), 39.5(C-15), 32.2 (C-19)
OMe-1	3.89, 3H s	56.9	56.9	56.9 (C-1)
OMe-10	3.88, 3H s	56.7	56.7	56.7 (C-10)
NMe-9	3.93, 3H s	35.2	35.2	130.4 (C-9a), 163.0 (C-8)
NMe-18	3.88, 3H s	34.8	34.8	130.6 (C-18a), 163.9 (C-17)

[a] = measured in 400 MHz, [b]= measured in 100 MHz, c = not observed

Table 2

^{1}H (H_a-H_g) and ^{13}C NMR data (400 MHz, $CDCl_3$) for compound **1**.

	Compound 1		**Vepridimerine A (Ngadjui et al., 1992)**	
Position	δ_H[a]	δ_C[b]	δ_H	δ_C
H_a	1.74 dt (*J* = 13.8, 2.5 Hz)	32.2	1.70 ddd (*J* = 13.7, 2.8, 2.2 Hz)	32.2
H_b	2.19 dd (*J* = 13.8, 2.8 Hz)	32.2	2.14 dd (*J* = 13.7, 2.7 Hz)	32.2
H_c	3.70 br s	27.8	3.61 ddd (*J* = 2.8, 2.7, 1.0 Hz)	26.2
H_d	2.23 d (*J* = 6.3 Hz)	43.5	2.16 dd (*J* = 6.1, 1.0 Hz)	43.6
H_e	3.05 ddd (*J* = 12.5, 6.0, 5.7 Hz)	26.5	2.96 ddd (*J* = 13.4, 6.1, 5.4 Hz)	27.6
H_f	3.20 ddd (*J* = 14.2, 5.5, 2.4 Hz)	39.5	3.10 ddd (*J* = 14.2, 5.4, 2.2 Hz)	39.5
H_g	1.57 t (*J* = 14.2 Hz)	39.5	1.56 dd (*J* = 14.2, 13.4 Hz)	39.5
[a] = measured in 400 MHz, [b]= measured in 100 MHz				

Compound **(2)**, ^{1}H NMR (400 MHz, $CDCl_3$): 7.76 dd (*J* = 8.0, 1.1 Hz, H-5), 7.20 ddd (*J* = 8.6, 8.0, 1.4 Hz, H-6), 7.48 ddd (*J* = 8.6, 8.4, 1.1 Hz, H-7), 7.30 d (*J* = 8.4 Hz, H-8), 3.34 d (2H, *J* = 7.0 Hz, H-1'), 5.20 t (*J* = 7.0 Hz, H-2'), 1.62, 3H s (Me-3'cis), 1.75, 3H s (Me-3'trans), 3.66, 3H s (N-Me), 3.85 3H s (OMe-4). ^{13}C (100 MHz, $CDCl_3$): 164.0 (C-2), 122.6 (C-3), 160.2 (C-4), 123.4 (C-5), 121.9 (C-6), 130.1 (C-7), 114.1 (C-8), 139.0 (C-9), 122.4 (C-10), 24.3 (C-1'), 121.5 (C-2'), 132.5 (C-3'), 25.7 (Me-3'*cis*), 19.0 (Me-3'*trans*) 29.8 (N-Me), 61.8 (OMe-4)

Compound (**3**), ^{1}H NMR (400 MHz, $CDCl_3$): 7.76 dd (*J* = 8.0, 1.1 Hz, H-5), 7.20 ddd (*J* = 8.6, 8.0, 1.4 Hz, H-6), 7.48 ddd (J = 8.6, 8.4, 1.1 Hz, H-7), 7.30 d (*J* = 8.4 Hz, H-8), 3.34 d (2H, *J* = 7.0 Hz, H-1'), 5.20 t (*J* = 7.0 Hz, H-2'), 1.62, 3H s (Me-3'*cis*), 1.75, 3H s (Me-3'*trans*), 3.66, 3H s (N-Me), 3.85, 3H s (OMe-4). ^{13}C (100 MHz, $CDCl_3$): 164.0 (H-2), 122.6 (H-3), 160.2 (H-4), 123.4 (H-5), 121.9 (H-6), 130.1 (H-7), 114.1(H-8), 139.0 (H-9), 122.4 (H-10), 24.3 (H-1'), 121.5 (H-2'), 132.5 (H-3'), 25.7 (Me-3'*cis*), 19.0 (Me-3'*trans*), 29.8 (N-Me), 61.8 (OMe-4)

Compound **(4)**, ^{1}H NMR (400 MHz, CD_3OD): 7.58 s (H-1), 8.31 s (H-4), 9.71 s (H-6), 7.99 d (*J* = 9.0 Hz, H-9), 8.67 d (*J* = 9.0 Hz, H-10), 8.67 d (*J* = 9.0 Hz, H-11), 8.24 d (*J* = 9.0 Hz, H-12), 4.28 3H s (OMe-7), 5.51 3H s (N-Me), 6.29 2H s (-OCH_2O-)

Compound **(5)** ^{1}H NMR (400 MHz, CDCl3): 7.32 s (H-1), 8.02 s (H-4), 10.72 s (H-6), 7.85 d (*J* = 9.0 Hz, H-9), 8.34 d (*J* = 9.0 Hz, H-10), 8.32 d (*J* = 9.0 Hz, H-11), 7.98 d (*J* = 9.0 Hz, H-12), 4.41 3H s (OMe-7), 4.04 3H s (OMe-8), 5.27 3H s (N-Me), 6.18 2H s (-OCH_2O-).

Compound **(6)**, ^{1}H NMR (400 MHz, $CDCl_3$): 7.82 s (H-1), 8.04 s (H-4), 10.72 s (H-6), 8.42 s (H-10, 8.23 d (*J* = 9.0 Hz, H-11), 7.85 d (*J* = 9.0 Hz, H-12), 4.41 3H s (OMe-7), 4.04 3H s (OMe-8), 3.88 3H s (OMe-9), 5.24 3H s (N-Me), 6.22 2H s (-OCH_2O-)

Compound (**7**), ^{1}H NMR (400 MHz, $CDCl_3$): 8.20 d (*J* = 5.9 Hz, H-1), 8.73 d (*J* = 5.9 Hz, H-2), 8.49 d (*J* = 10 Hz, H-4), 7.09 d (*J* = 10 Hz, H-5), 8.17 d (*J* = 8.0 Hz, H-8), 7.59 dd (*J* = 8.0, 7.5 Hz, H-9), 7.81 dd (*J* = 8.4, 7.5 Hz, H-10), 8.65 d (*J* = 8.4 Hz, H-11).

Compound (**8**), ^{1}H NMR (400 MHz, CDCl3): 6.97 d (*J* = 1.2 Hz, H-2), 6.71 d (*J* = 7.0, 9.0 Hz, H-5), 6.76 dd (*J* = 8.0,2.0 Hz, H-6), 4.66 d (*J* = 5.2 Hz, H-7), 3.09 m, H-8), 4.25 dd (*J* = 9.6, 6.0 Hz, H-9α), 3.94 m (H-9β), 6.83br s (H-2'), 6.74 d (*J* = 8.8 Hz, H-5'), 6.76 d (*J* = 8.0 Hz, H-6'), 4.44 d (*J* = 4 Hz, H-7'), 3.09 m (H-8'), 4.25 dd (*J* = 9.6, 6.0 Hz, H-9'α), 3.94 m (H-9'β), 3.80 3H s (OMe-3), 5.88 2H s (3',4'-OCH_2O-), 4.50 (*J* = 9.6 Hz, H-1"), 5.44 (*J* = 6 Hz, H-2"), 1.69 3H s (Me-3"*cis*), 1.65 3H s (Me-3"*trans*). ^{13}C (100 MHz, $CDCl_3$): 135.1 (C-1), 106.5 (C-2), 147.9 (C-3), 148.0 (C-4), 112.9 (C-5), 119.4 (C-6), 85.8 (C-7), 54.4 (C-8), 71.7 (C-9), 133.5 (C-1'), 109.4 (C-2'), 147.1 (C-3'), 149.8 (C-4'), 108.2 (C-5'), 118.2 (C-6'), 85.9 (C-7'), 54.1 (C-8'), 71.7 (C-9'), 56.0 (OMe-3), 101.1 (3',4'-OCH2O-), 65.8 (C-1"), 120.0 (C-2"), 137.6 (C-3"), 25.8 (Me-3"*cis*), 18.2 (Me-3"*trans*)

Molecular Docking with MPro

Molecular docking was performed on thirteen compounds to study their interactions with the Mpro (Table 3; Fig. 3) using AutoDock Vina The highest negative binding affinity is observed for compound **1** indicating that it can potentially serve as a chemical scaffold to develop a potent Mpro inhibitor .

Table 3
Non-covalent interactions of isolated compounds with Mpro (PDB ID 6LU7) (Pose predicted by AutoDock Vina)

Compound	Binding affinity	Hydrogen bond (AA...ligand)	Hydrophobic interaction (AA...ligand)	Electrostatic interaction (AA...ligand)
1	-8.5	GLY143 (2.601) C-H...O-C)	CYS145 (4.789) Alkyl	
		LEU141 (2.530) C-O...H-C)	MET49 (4.276) Alkyl	
		PHE140 (2.975) C-O...H-C)	MET49 (4.353) Alkyl	
		PHE140 (2.667) C-O...H-C	LEU27 (4.208) Alkyl	
		GLU166 (2.672) C-O...H-C	CYS145 (3.496) Alkyl	
			HIS163 (5.423) Pi-Alkyl	
8	-8	GLU166 (2.615) C-O...H-C)	HIS41 (5.823) Pi-Pi T-shaped	
			LEU27 (4.72) Alkyl	
			LEU27 (4.383) Alkyl	
			CYS145 (3.967) Alkyl	
			HIS41 (4.504) Pi-Alkyl	
			MET165 (5.479) Pi-Alkyl	
			ALA191 (5.124) Pi-Alkyl	
4	-7.8	ARG188 (2.792) C-H...O-C	GLU166 (2.687) Pi-Sigma	GLU166 (4.933) Pi-Anion
		HIS164 (2.549) C-O...H-C	MET165 (4.778) Pi-Alkyl	
		PHE140 (2.845) C-O...H-C	MET165 (4.741) Pi-Alkyl	
		GLU166 (2.613) C-O...H-C	MET49 (4.649) Pi-Alkyl	

Compound	Binding affinity	Hydrogen bond (AA...ligand)	Hydrophobic interaction (AA...ligand)	Electrostatic interaction (AA...ligand)
		GLU166 (3.047) Pi-Donor		
6	-7.6	ARG188 (2.784) C-H...O-C	GLU166 (2.745) Pi-Sigma	GLU166 (4.926) Pi-Anion
		HIS164 (2.509) C-O...H-C	MET165 (4.815) Pi-Alkyl	
		PHE140 (2.724) C-O...H-C	MET165 (4.753) Pi-Alkyl	
		GLU166 (2.755) C-O...H-C	MET49 (4.658) Pi-Alkyl	
		GLU166 (3.041) Pi-Donor		

Table 3 **(Cont.).** Non-covalent interactions of isolated compounds with Mpro (PDB ID 6LU7) (Pose predicted by AutoDock Vina)

Compound	Binding affinity	Hydrogen bond (AA...ligand)	Hydrophobic interaction (AA...ligand)	Electrostatic interaction (AA...ligand)
5	-7.5	ARG188 (2.480) C-O...H-C	PRO168 (2.537) Pi-Sigma	
		THR190 (2.758) C-O...H-C	MET165 (4.823) Alkyl	
			PRO168 (4.537) Pi-Alkyl	
			MET165 (5.086) Pi-Alkyl	
9	-7.2	SER144 (2.737) O-H...O-C	ALA191 (3.775) Alkyl	
		LEU141 (2.757) C-O...H-O	PRO168 (4.205) Alkyl	
			PRO168 (3.972) Alkyl	
10	-6.7	SER144 (2.710) C-H...O-C	ALA191 (4.156) Alkyl	
			PRO168 (4.156) Alkyl	

Compound	Binding affinity	Hydrogen bond (AA...ligand)	Hydrophobic interaction (AA...ligand)	Electrostatic interaction (AA...ligand)
2	-6.3		HIS41 (4.917) Pi-Pi T-shaped	
			MET165 (4.480) Alkyl	
			HIS163 (4.690) Pi-Alkyl	
			HIS172 (5.434) Pi-Alkyl	
			MET165 (4.759) Pi-Alkyl	
			MET165 (5.048) Pi-Alkyl	
3	-6.1		CYS145 (4.795) Alkyl	
			MET49 (5.120) Alkyl	
			CYS145 (4.953) Alkyl	
			HIS41 (3.736) Pi-Alkyl	
			HIS163 (4.672) Pi-Alkyl	
			HIS163 (4.793) Pi-Alkyl	
			HIS172 (4.905) Pi-Alkyl	
			MET165 (4.428) Pi-Alkyl	
			MET165 (4.063) Alkyl	
			HIS41 (4.707) Pi-Alkyl	
			HIS41 (4.680) Pi-Alkyl	

Molecular interaction of the four compounds with Mpro

Non-covalent interactions are known to play a major role as they are considered to drive protein-ligand interaction (Chen & Kurgan 2009). A number of non-covalent interactions for example hydrogen bond and hydrophobic interactions are found to be involved in the binding of the compounds with Mpro when the poses were estimated with AutoDock Vina (Fig. 3 and Fig. 4). Among the thirteen compounds, the highest negative binding affinity was observed for compound **1** (-8.5 kcal/mol). Compound **1** formed five hydrogen bonds and six hydrophobic bonds with Mpro. In compound **8**-Mpro complex, the complex was stabilized by one hydrogen bond and seven hydrophobic bonds. The compound **4**-Mpro complex formed a stable network by five hydrogen bonds, four hydrophobic bonds and one electrostatic bond whereas in compound **5**-Mpro complex, five hydrogen bonds, four hydrophobic bonds, and one electrostatic bond were detected (Fig. 4). Similar interactions were shown by the rest eight compounds with Mpro (Table 3 and Fig. 5).

Result obtained from Molecular dynamics simulation

For the promising Mpro inhibitors, we conducted molecular dynamics, and explored the MD stability of each MD system. MD simulation for complex of Mpro with new compound **1** was performed for 100 ns. Apo form and an available drug, remdesivir along with Mpro were also employed for MD run. In place of compound **1**, the RMSDs (0.4–2.4 Å) for α-carbon atoms is lower than remdesivir (0.4–2.5 Å) and apo form (0.4–2.7 Å), thus suggesting that the compound **1** can be more stable in physiological conditions. In Fig. 6A, RMSD values of compound **1** are slightly increased to 2.1 Å after 22 ns and showed few smaller fluctuations at 26, 74 and 82 ns. Apart from this, the trajectories generated throughout the whole run were stable. Thus, higher structural stability in the Mpro-compound **1** complex is identified. On the other hand, the RMSD of remdesivir and Apo exhibit similar higher fluctuations over the whole run and is expanded to 2.7 Å in both cases. The average RMSD for compound **1** and remdesivir is 1.6 Å and 1.7 Å, whereas for apo detected around 2.1 Å. It is indicated that the both compounds can be a stable and compound **1** can be the best inhibitor.

Root mean square fluctuations (RMSF) property is highly used to capture the conservation of protein dynamics (Fuglebakk, Echave and Reuter, 2012). The highest degree of flexibility is detected for apo-Mpro, whereas a similar fluctuation (average 1.2 Å) is noticed for compound **1**-Mpro and remdesivir-Mpro. The less fluctuation indicates higher protein structural stability. In addition, the visual analysis of MD simulation trajectories proposes that compound **1** involved in major binding interactions with the hotspot residues (HIS163, GLU166, CYS145, GLY143, HIS172, PHE140, HIS41, THR25, MET49, MET165, and GLN189) of the Mpro protein (Fig. 6B).

The radius of gyration is a parameter that indicates protein structural compactness. During the simulation run a lower degree of fluctuation with its consistency suggests the greater compactness and rigidity of the system (Lobanov, Bogatyreva, & Galzitskaya, 2008). Throughout the whole run a bigger radius of gyration is identified for compound **1** than remdesivir that proposes comparatively loose packing of the compound 1-protein complex. Though the average (22.3 Å) is the same for compound 1 and apo form, more than remdesivir (average 22.1 Å), indicates both can be potential inhibitors (Fig. 6C).

The expansion of protein volume is indicated by higher solvent-accessible surface area (SASA) value and a low fluctuation is anticipated all through the simulation time. The assessment of SASA indicates the highest value for apo form (average 14160 Å²) whereas compound 1-Mpro complex (average 14000 Å²) and remdesivir (average 13847 Å²) (Fig. 6D). It was also determined molecular surface area (MolSA) for the drug-protein complexes. In this exploration, Compound 1 reveals high MolSA (average 14027 $Å^2$) than remdesivir, average 13952 $Å^2$ (Fig. 7A). A remarkable difference is detected for dihedral angles of compound 1 (average 70261) (Fig. 7B) compared to those of the standard, remdesivir (average 70810). Hydrogen bonds show a vital role in molecular recognition and the whole stability of the protein structure. During the whole 100ns, the formed intermolecular hydrogen bonds is composed from the trajectories. Compound 1 showed the highest number of hydrogen bonds with Mpro (average 509) (Fig. 7C).

Binding free energy analysis

For understanding how the structural changes influence ligand binding each snapshot was subjected to MM-PBSA calculation. The binding free energy of each snapshot containing protein-ligand complex is shown in Fig. 7D. On average, the binding free energy of remdesivir was calculated to be highest, which was about 21.85 KJ/mol. For this complex, the greater free energy of binding was observed at 66.8 ns and 84.3 ns, which was calculated as 102.24 KJ/mol, and 118.66 KJ/mol, respectively. On the contrary, the average binding free energy of compound 1 was calculated as -23.74 KJ/mol. It showed greater free energy of binding at 89.9 ns, and 93.5 ns, which was calculated as 69.53 KJ/mol, and 74.73 KJ/mol respectively.

Compound **1** indicated the highest binding affinity of -8.5 kcal/mol. When docking results are considered with the other three compounds, together with hydrogen bond and hydrophobic bonds compound 1 shows very strong binding interactions with the important amino acids of Mpro (Nishimasu et al., 2011, Stein et al., 2015). Compared to the others, through hydrogen bond and alkyl interactions it also showed better and more appropriate interactions with the significant residues. It can promote more interactions than the others, contributing to a higher binding affinity. Amino acid residues, MET49, CYS145, GLU166, HIS163 and MET165 in the catalytic domain of Mpro were found to participate in non-covalent interactions with most of the compounds (Fig. 4 and Table 3). By MD simulation compound **1** displayed the average RMSD values (1.6 Å) which is lower compared to remdesivir (1.9 Å), representing more structural stability with Mpro in bound states. From the RMSF values it was observed that compound **1** had more acceptable binding stability with Mpro (Fig. 6B), demonstrates important interaction with significant residues showed their compactness in a complex form with Mpro. Both the compound 1 and remdesivir complexes were found to be similar and stable (Fig. 6C and Fig. 6D) that was revealed by the Rg and SASA values. Furthermore, the compound 1-Mpro complex displays the higher value than remdesivir MolSA value (Fig. 7A). All analyses from the MD simulations support the docking results signifying that our isolated compound **1** (2,11-didemethoxy-vepridimerine A) can inhibit the activity of Mpro of SARS-Cov-2.

Discussion

In this stidy we identfied a a new natural compound 2,11-didemethoxy-vepridimerine A (1), the dimeric prenylated quinolone alkaloid, that showed promising interaction with SARS-CoV-2 Mpro. Mpro, coronavirus main protease, is a critical enzyme mediating the production of CoV functional proteins.the molecular docking results were supported by the MD simulation calculations. This suggest that the isolated compound 1 can potentially inhibit the activity of Mpro, and can be used as a lead compound for an Mpro targeting drug-discovery programme. However, this results need to be validated using in vitro wet lab experiments to fully understand the potential utlity of this chemical class.

Declarations

Conflicts of Interest

The authors declare no conflict of interest.

Acknowledgements

We would like to thank to Phytochemical Research Lab, Pharmaceutical Chemistry Department, Dhaka University for the support of chemical isolation of plant extract as well as Bangladesh Council of Scientific and Industrial Research (BCSIR), Dr. Qudrat-E-Khuda Road, Dhaka 1205, Bangladesh. The authors wish to gratefully acknowledge Dr. Mohammad A. Halim and Division of Computer Aided Drug Design, The Red-Green Research Centre for cordial support to this research. This research received no external funding.

References

Ahmed, S., Islam, N., Shahinozzaman, M., Fakayode, S.O., Afrin, N. and Halim, M.A., 2021. Virtual screening, molecular dynamics, density functional theory and quantitative structure activity relationship studies to design peroxisome proliferator-activated receptor-γ agonists as anti-diabetic drugs. *Journal of Biomolecular Structure and Dynamics*, *39*(2), pp.728-742. https://doi.org/10.1080/07391102.2020.1714482

Atanasov, A.G., Waltenberger, B., Pferschy-Wenzig, E.M., Linder, T., Wawrosch, C., Uhrin, P., Temml, V., Wang, L., Schwaiger, S., Heiss, E.H. and Rollinger, J.M., 2015. Discovery and resupply of pharmacologically active plant-derived natural products: A review. *Biotechnology advances*, *33*(8), pp.1582-1614. https://doi.org/10.1016/j.biotechadv.2015.08.001

Chen, K. and Kurgan, L., 2009. Investigation of atomic level patterns in protein—small ligand interactions. *PLoS One*, *4*(2), p.e4473. https://doi.org/10.1371/journal.pone.0004473

DeLano, W.L., 2002. Pymol: An open-source molecular graphics tool. *CCP4 Newsl. Protein Crystallogr*, *40*(1), pp.82-92. http://www. pymol. org.

Frisch, M.J., 2009. gaussian09. *http://www. gaussian. com/*.

Fuglebakk, E., Echave, J. and Reuter, N., 2012. Measuring and comparing structural fluctuation patterns in large protein datasets. *Bioinformatics*, 28(19), pp.2431-2440. https://doi.org/10.1093/bioinformatics/bts445

Guex, N. and Peitsch, M., 1997. SWISS-MODEL and the Swiss-Pdb Viewer: An environment for comparative protein modeling. *Electrophoresis*, 18(15), pp.2714-2723. https://doi.org/10.1002/elps.1150181505

Hasan, C., Ahmed, N., Haque, R., Haque, M., Begum, S., Sohrab, M. and Ahsan, M., 2013. Secondary metabolites from the stem of Ravenia spectabilis Lindl. *Pharmacognosy Magazine*, 9(33), p.76. https://doi.org/10.4103/0973-1296.108147

Islam, M., Khan, A., Parves, M., Hossain, M. and Halim, M., 2019. Prediction of Deleterious Non-synonymous SNPs of Human STK11 Gene by Combining Algorithms, Molecular Docking, and Molecular Dynamics Simulation. *Scientific Reports*, 9(1).

Islam R., Parves M.R., Paul A.S., Uddin N., Rahman M.S., Mamun A.A., Hossain M.N., Ali M.A. & Halim M.A. (2021) A molecular modeling approach to identify effective antiviral phytochemicals against the main protease of SARS-CoV-2. Journal of Biomolecular Structure and Dynamics 39, 3213-24. https://doi.org/10.1080/07391102.2020.1761883

Sonju, J., Anwar, M., Azad, M., Sultana, U., Niloy, K. and Das, S., 2021. Antiviral Effects of Asian Natural Products Targeting SARS, MERS, and COVID-19. *Coronaviruses*, 2(7). https://doi.org/10.2174/2666796702666210127111918

Junaid M., Islam N., Hossain M.K., Ullah M.O. & Halim M.A. (2019) Metal based donepezil analogues designed to inhibit human acetylcholinesterase for Alzheimer's disease. PloS one 14, e0211935. https://doi.org/10.1371/journal.pone.0211935

Khan, A.M., Shawon, J. and Halim, M.A., 2017. Multiple receptor conformers based molecular docking study of fluorine enhanced ethionamide with mycobacterium enoyl ACP reductase (InhA). *Journal of Molecular Graphics and Modelling*, *77*, pp.386-398. https://doi.org/10.1016/j.jmgm.2017.09.010

Krieger, E., Darden, T., Nabuurs, S.B., Finkelstein, A. and Vriend, G., 2004. Making optimal use of empirical energy functions: force-field parameterization in crystal space. *Proteins: Structure, Function, and Bioinformatics*, *57*(4), pp.678-683. https://doi.org/10.1002/prot.20251

Mlu, L., Bogatyreva, N.S. and Galzitskaia, O.V., 2008. Radius of gyration is indicator of compactness of protein structure. *Molekuliarnaia biologiia*, *42*(4), pp.701-706. PMID: 18856071

Ngadjui, B.T., Ayafor, J.F., Bilon, A.N., Sondengam, B.L., Connolly, J.D. and Rycroft, D.S., 1992. Synthesis of veprisine dimers and the formation of a novel cyclic tetramer from precocene I. *Tetrahedron*, *48*(40),

pp.8711-8724. https://doi.org/10.1016/S0040-4020(01)89446-1

Ngadjui, T.B., Ayafor, J.F., Sondengam, B.L., Connolly, J.D., Rycroft, D.S., Khalid, S.A., Waterman, P.G., Brown, N.M., Grundon, M.F. and Ramachandran, V.N., 1982. The structures of vepridimerines AD, four new dimeric prenylated quinolone alkaloids from Vepris lousii and Oricia renieri (Rutaceae). *Tetrahedron Letters*, *23*(19), pp.2041-2044. https://doi.org/10.1016/S0040-4039(00)87255-X

Nishimasu, H., Okudaira, S., Hama, K., Mihara, E., Dohmae, N., Inoue, A., Ishitani, R., Takagi, J., Aoki, J. and Nureki, O., 2011. Crystal structure of autotaxin and insight into GPCR activation by lipid mediators. *Nature structural & molecular biology*, *18*(2), pp.205-212. https://doi.org/10.1038/nsmb.1998

Osakwe, O. and Rizvi, S.A.A., 2016. The significance of discovery screening and structure optimization studies. *Social aspects of drug discovery, development and commercialization*, pp.109-128. https://doi.org/10.1016/B978-0-12-802220-7.00005-3

Shahinozzaman, M., Ishii, T., Ahmed, S., Halim, M.A. and Tawata, S., 2020. A computational approach to explore and identify potential herbal inhibitors for the p21-activated kinase 1 (PAK1). *Journal of Biomolecular Structure and Dynamics*, *38*(12), pp.3514-3526. https://doi.org/10.1080/07391102.2019.1659855

Sharma, A., Tiwari, S., Deb, M.K. and Marty, J.L., 2020. Severe acute respiratory syndrome coronavirus-2 (SARS-CoV-2): a global pandemic and treatment strategies. *International journal of antimicrobial agents*, *56*(2), p.106054. https://doi.org/10.1016/j.ijantimicag.2020.106054

Stein, A.J., Bain, G., Prodanovich, P., Santini, A.M., Darlington, J., Stelzer, N.M., Sidhu, R.S., Schaub, J., Goulet, L., Lonergan, D. and Calderon, I., 2015. Structural basis for inhibition of human autotaxin by four potent compounds with distinct modes of binding. *Molecular pharmacology*, *88*(6), pp.982-992. https://doi.org/10.1124/mol.115.100404

Thomford, N.E., Senthebane, D.A., Rowe, A., Munro, D., Seele, P., Maroyi, A. and Dzobo, K., 2018. Natural products for drug discovery in the 21st century: innovations for novel drug discovery. *International journal of molecular sciences*, *19*(6), p.1578. https://doi.org/10.3390/ijms19061578

Yonesi, M. and Rezazadeh, A., 2020. Plants as a prospective source of natural anti-viral compounds and oral vaccines against COVID-19 coronavirus. https://doi.org/10.20944/preprints202004.0321.v1

Figures

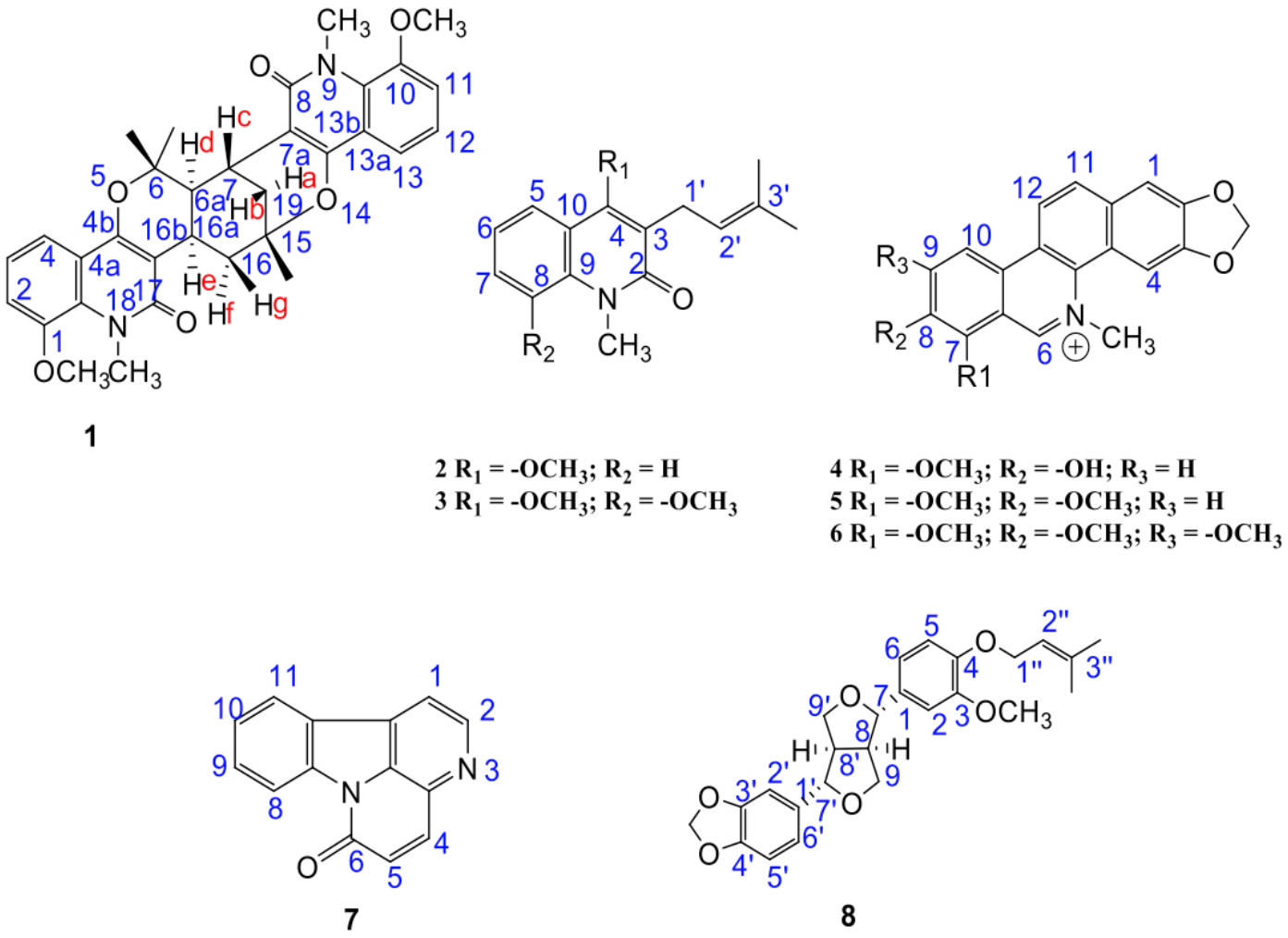

Figure 1

Structures of the compounds isolated from *Zanthoxylum rhetsa.*

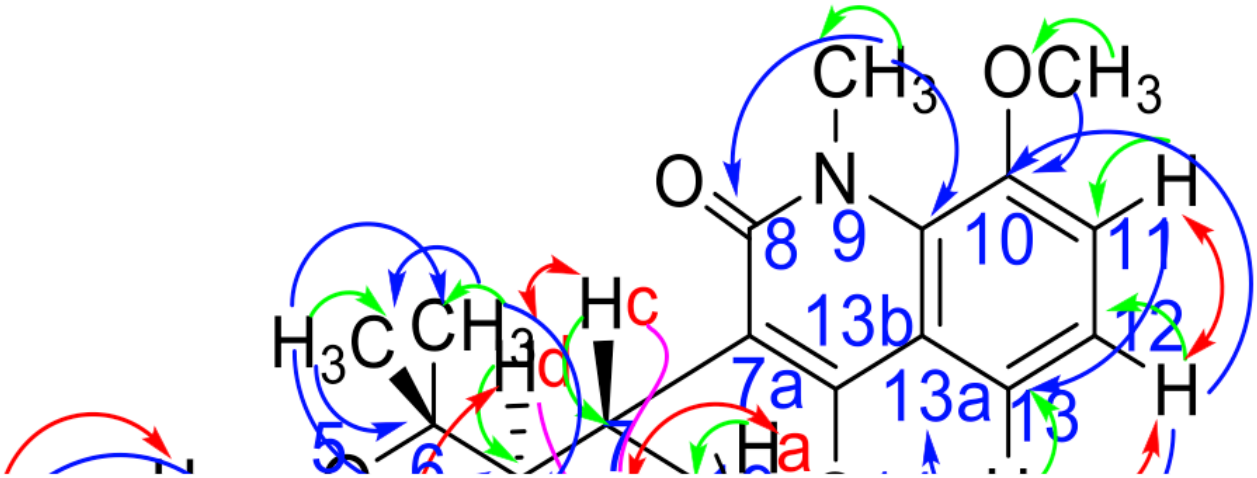

Figure 2

Key COSY (red), HSQC (green), HMBC (blue) and NOESY (pink) correlations for Compound 1

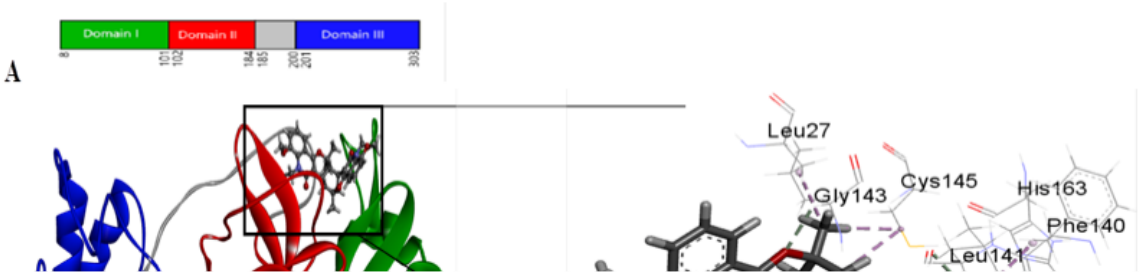

Figure 3

(A) Schematic 1D amino acid sequence of main protease. (B) Interaction of main protease with Compound **1** (c) Interaction of main protease with different Compound and binding affinity

Figure 4

Domain organization and interaction of Mpro with 4 compounds. (A) The interdomain borders are labeled with amino acid residue numbers. (B) Three dimensional representation of Mpro (Domain I-Green; Domain II-Red; Domain III-Blue) interacting with 4 compounds. Here Compound 1- Cyan; Compound 8- Magenta; Compound 4- Yellow; Compound 5- Orange.

Figure 5

Non-bonding interactions of different compounds with Mpro (Pose predicted by AutoDock Vina)

Figure 6

(A) Root mean square deviation values of C-α atom of Mpro in the complexes with compound 1 and Remdesivir along the 100 ns MD simulations. The structural changes of Mpro by means of (B) root means square fluctuations, (C) solvent accessible surface area, and (D) radius of gyration formed during the simulation

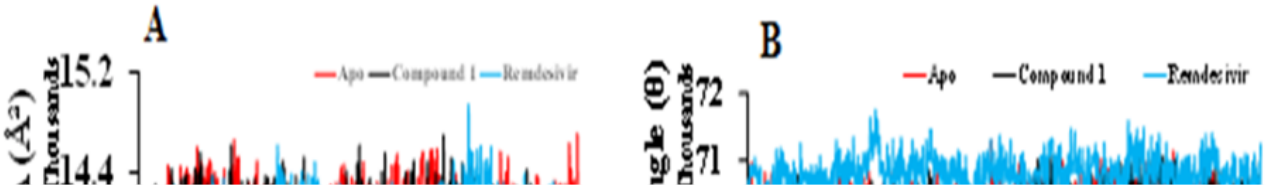

Figure 7

(A) Molecular surface area value of Mpro in the complexes with compound 1 and Remdesivir along the 100 ns MD simulations. The structural changes of Mpro by means of (B) dihedral angle, (C) total number of H bonds formed during the simulation, and (D) binding free energy analysis of Compound 1 and Remdesivir complex

Supplementary Files

This is a list of supplementary files associated with this preprint. Click to download.

- SupplementaryMaterialZR.pdf